X-ray spectroscopic and first-principles investigation of lead tungstate under pressure

J. M. Ablett,[1] S. R. Shieh,[2,3] V. Balédent,[4] J. C. Woicik,[5] E. Cockayne,[5] and E. L. Shirley[6]

[1]*Synchrotron Soleil, L'Orme des Merisiers, BP 48, Saint Aubin, 91192 Gif-sur-Yvette, France*
[2]*Department of Earth Sciences, University of Western Ontario, London, Ontario, N6A 5B7, Canada*
[3]*Department of Physics and Astronomy, University of Western Ontario, London, Ontario, N6A 5B7, Canada*
[4]*Université Paris-Saclay, CNRS, Laboratoire de Physique des Solides, 91405, Orsay, France*
[5]*Materials Measurement Science Division, Material Measurement Laboratory, National Institute of Standards and Technology, Gaithersburg, Maryland 20899, USA*
[6]*Sensor Science Division, Physical Measurement Laboratory, National Institute of Standards and Technology, Gaithersburg, Maryland 20899, USA*

(Received 15 December 2020; revised 8 June 2021; accepted 5 August 2021; published 26 August 2021)

High-energy-resolution fluorescence-detected (HERFD) near-edge x-ray-absorption fine-structure measurements performed at the Pb and W L_3 absorption edges have been used to study the pressure dependence of the local atomic structure of $PbWO_4$ from 1 bar up to 22 GPa. Comparison of measured spectra with density-functional theory structural calculations and simulations based on solution of the Bethe-Salpeter equation establish an unambiguous $PbWO_4$-I to $PbWO_4$-III phase transition around 7 GPa. No evidence of either the Raspite or Fergusonite structures is found. The smaller core-hole lifetime broadening afforded by HERFD allows unique experimental determination of crystal-field splitting and its sensitivity to the oxygen cage geometry surrounding the Pb and W atoms thus giving definitive identification of the high-pressure phase of $PbWO_4$.

DOI: 10.1103/PhysRevB.104.054119

I. INTRODUCTION

Lead tungstate ($PbWO_4$) is a popular material for scintillating detectors and is also used in calorimeters found in high-energy particle physics experiments [1] and Raman lasers [2]. It has a strong radiation hardness and fast decay time (<25 ns), it scintillates at visible wavelengths (about 420 nm) and it is relatively inexpensive to produce. Furthermore, its optical properties can be tuned by doping or by changing the growth morphology such as in the fabrication of nanorods [3]. Structurally, $PbWO_4$ naturally occurs in two forms: $PbWO_4$-I (stolzite, which has the scheelite structure, featuring WO_4 tetrahedra), and $PbWO_4$-II (Raspite, featuring overlapping WO_6 octahedra). $PbWO_4$-II is the less common form but can be produced synthetically [4,5]. A lead-deficient phase of $PbWO_4$ has also been reported [6], and a monoclinic form known as $PbWO_4$-III (also featuring overlapping WO_6 octahedra) can be grown by quenching following a high-pressure, high-temperature treatment [7,8]. This $PbWO_4$-III structure reverts back to $PbWO_4$-I upon grinding [7].

Under ambient conditions, crystallization of $PbWO_4$-I in the body-centered tetragonal scheelite crystal structure is confirmed by neutron- [9,10] and x-ray-diffraction studies [10]. It is an insulator with a band-gap of approximately 4 eV [11,12]. This structure can be viewed as Pb^{2+} atoms ionically bonded to $(WO_4)^{2-}$ anions, where the W^{6+} cations are fourfold covalently bonded to the oxygen atoms forming distinct rigid tetrahedra with W-O distances of between 2.7 and 3.2 Å. The compressibility of $PbWO_4$-I is mainly attributed to compression along the c axis [13]. There have been several experimental studies of the ambient-temperature, high-pressure phases of $PbWO_4$ [10,11,14–18]. These studies have determined high-pressure phases that consist of either a monoclinic-distorted form with the Fergusonite-type structure or a monoclinic $PbWO_4$-III phase wherein the tungsten atoms are octahedrally coordinated to their oxygen neighbors. Although the most recent results of Raman scattering [18], UV-visible optical absorption, and electronic structure calculations [11,19] suggest a single phase transition at around 7 GPa from $PbWO_4$-I directly to $PbWO_4$-III, the determination of this high-pressure phase has not been conclusively proven.

In this work, we measure pressure-dependent high-resolution x-ray absorption spectra (XAS) of $PbWO_4$ at both the Pb and W L_3 absorption edges. The spectra are analyzed using a combination of structural optimization based on density-functional theory (DFT) (for $PbWO_4$-I, $PbWO_4$-II, $PbWO_4$-III and the Fergusonite-type phase) and simulated absorption spectra found by solving the Bethe-Salpeter equation for the theoretically determined structures. We compare theoretical enthalpies of formation for various phases at different pressures and measured versus predicted spectral features at various pressures. The combined results confirm the above-mentioned, $PbWO_4$-I to $PbWO_4$-III single phase transition.

II. EXPERIMENT

We used the high-energy-resolution fluorescence-detected (HERFD) technique [20–23] to suppress $2p$ core-hole lifetime broadening of measured Pb and W $2p$ excitation spectral features. Measurements were performed at the GALAXIES inelastic-scattering undulator beamline at the SOLEIL synchrotron radiation facility [24,25]. A schematic of the experimental layout is shown in Fig. 1.

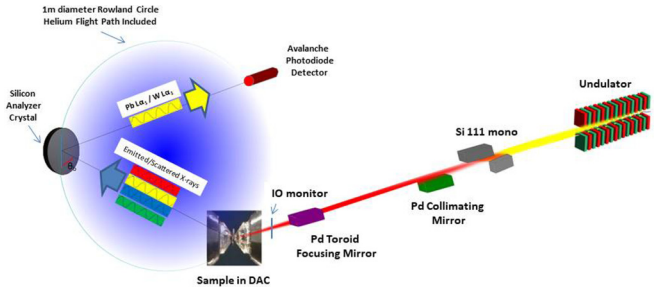

FIG. 1. Experimental layout: The undulator x-ray radiation is monochromatized by a Si(111) monochromator, collimated by a Pd mirror, and subsequently focused at the sample in a diamond-anvil cell, by a toroidal mirror. W and Pb Lα_1 fluorescence photons emitted along the entire sample length are discriminated by the silicon analyzer and collected by an avalanche photodiode. The sample, analyzer, and detector are all situated on a 1m diameter Rowland circle in the vertical scattering plane. The incident x-ray intensity (IO) is monitored just upstream from the sample position.

Finely ground $PbWO_4$ powder was obtained from a single crystal grown by the Czochralski technique from the same batch as was studied by Jayaraman *et al.* [26]. The powder was loaded into a membrane-driven diamond anvil cell (DAC) using a 30-μm-thick stainless steel gasket, with a hole of 150 μm. Silicone oil was used as a pressure-transmitting medium which ensured quasihydrostatic conditions up to at least 15 GPa [27,28]. Furthermore, the use of a finely ground powder sample dispersed in a pressure-transmitting medium will suppress the microstresses within the sample and is thus less sensitive to nonhydrostatic effects inside the DAC compared to a single-crystal counterpart under exactly the same conditions [29]. The cell consisted of 1.3 mm-thick, 300 μm-wide diamond culets and the pressure within the cell was varied by increasing the gas pressure on a membrane connected to one of the diamond anvils. A few micron-sized ruby chips were also loaded into the cell and used to determine the pressure by following the pressure induced energy shifts of the ruby fluorescence lines [30].

The incident synchrotron beam was monochromatized using a nitrogen-cooled, Si(111) fixed-exit double-crystal monochromator, followed by a Pd-coated spherical collimating mirror. The x-rays were then focused to a spot size of 30 μm (vertical) by 90 μm (horizontal) full width at half maximum (FWHM) at the sample position by a 3:1 toroidal Pd-coated mirror. The W and Pb Lα_1 x-ray emissions (8398 and 10552 eV, respectively) were monitored by 1 m-radius Si(444) and Si(555) spherically bent crystal analyzers (two of each) reflecting onto a Si avalanche-diode detector. The total instrumental resolution, due to the x-ray monochromator and spectrometer analyzer-crystal bandwidths, was measured to be approximately 2.0 eV FWHM at both the W and Pb L_3 absorption edges, as determined by the quasielastic scattering profile from a thin polyimide foil. The incident x-ray flux was approximately 1×10^{13} photons/s on the sample as determined from the photon-induced electron current in a silicon photodiode. The incident x-ray energy was scanned across the W and Pb L_3 absorption edges (10207 and 13035 eV, respectively) while monitoring both the incident-beam (from the integrated intensity from a quad beam-position monitor fitted with a 500-nm-thick Ti foil upstream of the sample position) and the emitted fluorescence intensity as described above.

The sample, analyzer crystals, and diode detector were all arranged in a vertical-scattering Rowland-circle geometry. The experiment was performed in a transmission geometry and helium flight paths were used to maximize flux by

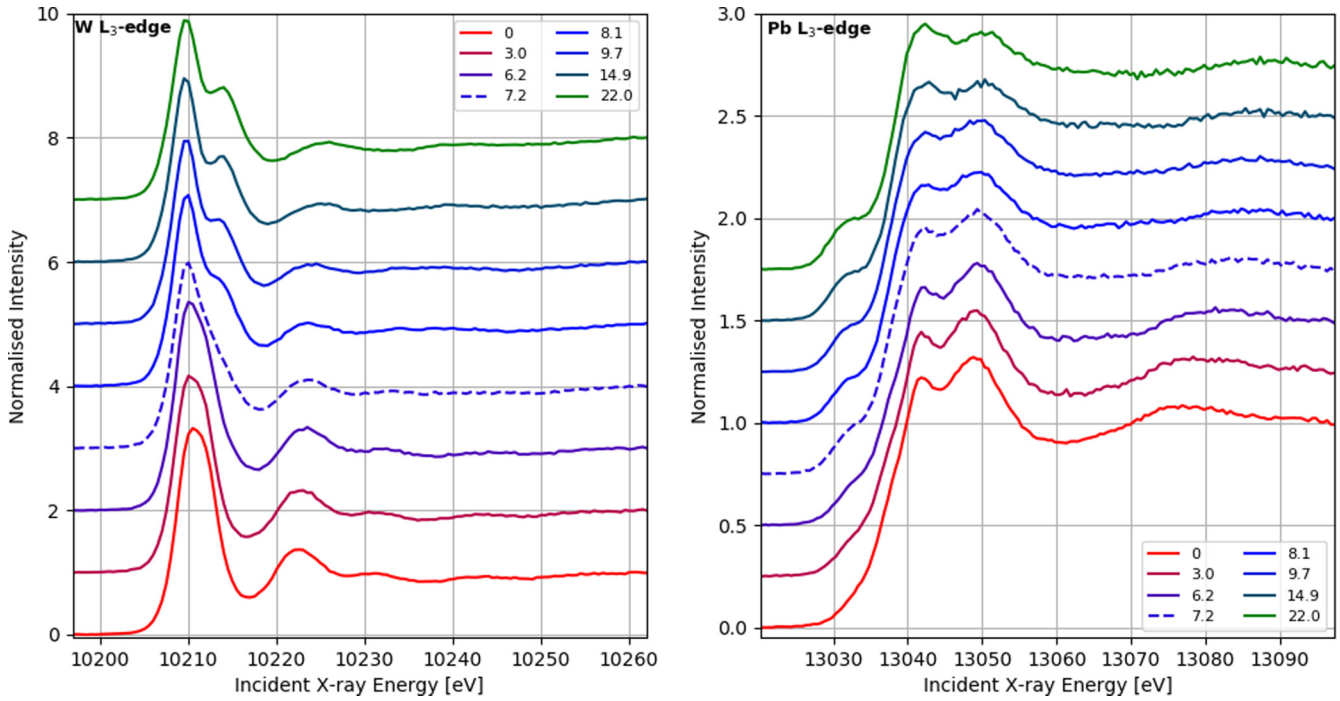

FIG. 2. (Left/Right panels) W/Pb L_3 near-edge experimental HERFD spectra of $PbWO_4$ for several values of applied pressure from 0 GPa (1bar) up to 22 GPa at room temperature. Line colors indicate measured pressures (in GPa) as shown in the inset legends.

TABLE I. Comparison between published crystal structural parameters for $PbWO_4$-I [19], $PbWO_4$-III [19], Fergusonite-type [19], $PbWO_4$-II [50] and those from our DFT calculations.

		Published structures			This work		
		$PbWO_4$-I at 0.7 GPa (Rietveld refinement) [19] $I4_1/a$, $Z = 4$, $a = 5.436$ Å, $c = 11.957$ Å			DFT $PbWO_4$-I DFT at 0.7 GPa (optb86bvdw+SCAN average) $a = 5.4650$ Å, $c = 11.9418$ Å		
Atom	Site	x	y	z	x	y	z
Pb	4b	0	0.25	0.625	0	0.25	0.625
W	4a	0	0.25	0.125	0	0.25	0.125
O	16f	0.2482	0.1073	0.051	0.2321	0.1043	0.0415
		$PbWO_4$ (Fergusonite-type structure) at 9.5 GPa (DFT-PBE) [19] $I2/a$, $Z = 4$, $a = 5.900$ Å, $b = 11.090$ Å, $c = 4.923$ Å, $\beta = 96.601°$			DFT $PbWO_4$ (Fergusonite-type structure) at 9.5 GPa (optb86bvdw+SCAN average) $I2/a$, $Z = 4$, $a = 5.9067$ Å, $b = 10.9191$ Å, $c = 4.8724$ Å, $\beta = 97.162°$		
Atom	Site	x	y	z	x	y	z
Pb	4e	0.25	0.6175	0	0.25	0.6184	0
W	4e	0.25	0.1521	0	0.25	0.1519	0
O_1	8f	0.9049	0.9554	0.2246	0.9061	0.9573	0.2258
O_2	8f	0.4528	0.2126	0.7674	0.4506	0.2110	0.7628
		$PbWO_4$-II at ambient pressure [50] $P2_1/a$, $Z = 4$, $a = 13.555$ Å, $b = 4.976$ Å, $c = 5.561$ Å, $\beta = 107.63°$			DFT $PbWO_4$-II (optb86bvdw+SCAN average) $P2_1/a$, $Z = 4$, $a = 13.6364$ Å, $b = 4.9845$ Å, $c = 5.5926$ Å, $\beta = 107.964°$		
Atom	Site	x	y	z	x	y	z
Pb	4e	0.14961	0.19405	0.16670	0.1516	0.1964	0.1667
W	4e	0.07708	0.74944	0.61185	0.0773	0.7494	0.6122
O_1	4e	0.0163	0.0515	0.7290	0.0179	0.0453	0.7289
O_2	4e	0.0595	0.4346	0.3882	0.0617	0.4422	0.3925
O_3	4e	0.1510	0.6148	0.9000	0.1493	0.6167	0.9128
O_4	4e	0.1903	0.8829	0.5386	0.1870	0.8930	0.5393
		$PbWO_4$-III at 12 GPa [19] $P2_1/n$, $Z = 8$, $a = 12.2171$ Å, $b = 6.8146$ Å, $c = 7.2069$ Å, $\beta = 89.63°$			$PbWO_4$-III at 12 GPa (optb86bvdw+SCAN average) $P2_1/n$, $Z = 8$, $a = 12.0896$ Å, $b = 6.7836$ Å, $c = 7.1846$ Å, $\beta = 89.354°$		
Atom	Site	x	y	z	x	y	z
Pb_1	4e	0.1591	0.6760	0.1645	0.1593	0.6775	0.1655
Pb_2	4e	0.1356	0.9576	0.6238	0.1339	0.9610	0.6255
W_1	4e	0.0850	0.1680	0.0824	0.0857	0.1687	0.0803
W_2	4e	0.0968	0.4637	0.6444	0.0977	0.4670	0.6438
O_1	4e	0.1036	0.0197	0.2883	0.1045	0.0200	0.2863
O_2	4e	0.1941	0.6057	0.7748	0.1966	0.6083	0.7717
O_3	4e	0.0474	0.6587	0.4739	0.0467	0.6611	0.4742
O_4	4e	0.2228	0.2676	0.0661	0.2240	0.2703	0.0666
O_5	4e	0.0663	0.2606	0.8137	0.0680	0.2616	0.8126
O_6	4e	0.1836	0.3375	0.4863	0.1845	0.3423	0.4826
O_7	4e	0.0209	0.3894	0.1801	0.0203	0.3890	0.1795
O_8	4e	0.0824	0.9126	0.9489	0.0835	0.9125	0.9483

eliminating the effects of air absorption and reduce background by air scattering. The sample thickness was estimated to be approximately 10 μm by its x-ray transmission across the W L_3 absorption edge. Room temperature HERFD spectra were recorded from 1 bar up to 15 GPa in approximately 1 GPa pressure steps with two additional high-pressure points at about 17 and 22 GPa. Data treatment consisted of subtracting a small constant background from the data and normalizing the edge step to unity. No self-absorption corrections were applied to the fluorescence data [31] because simulations, using the 10-μm sample thickness, accounted for at most a 10% decrease in intensity for the strong tungsten white line, and could be safely ignored.

III. EXPERIMENTAL RESULTS

Selected W and Pb L_3 HERFD near-edge spectra are shown in Fig. 2. For the W L_3 absorption edge (Fig. 2, left panel), leading spectral features indicate empty W 6s and, most importantly, 5d states as evidenced by the intense tungsten white

TABLE II. Comparative $PbWO_4$ phase stability using different density functionals. The LDA and PW91 functional results are taken from the literature whereas the other functionals (*) are our own work. $P = 0$ refers to ambient pressure results. I, II and III denote the $PbWO_4$-I, $PbWO_4$-II and $PbWO_4$-III phases respectively. $H_{II} - H_I$ is the enthalpy difference between $PbWO_4$-I and $PbWO_4$-II.

	Functional				
	LDA [4]	PW91 [19]	PBE*	optB86bvdW*	SCAN*
Low-Pressure ($P = 0$) phase	II	I	II	II	I
H_{II}-H_I ($P = 0$) (meV/ atom)			−4.1	−8.7	3.9
Low-Pressure ($P = 0$) phase to III transition pressure (GPa)	1.8	5	5.1	1.4	3.1
I to III transition pressure (GPa)		5	4.7	0.4	3.1
I to FergusoniteFergusonite-type structure transition pressure (GPa)		8	7.8	3.4	7.7

line. Subtle changes are observed with increasing pressure from 0 GPa (1 bar) up to 6.2 GPa, while a dramatic change occurs by 7.2 GPa. We tentatively attribute this dramatic change to a $PbWO_4$-I to $PbWO_4$-III phase transition, consistent with high-pressure Raman scattering measurements [18]. Otherwise, changes in the near-edge spectra are quite weak as the pressure varies on either side of the phase transition, so that the occurrence of a given phase might be established or ruled out for a range of pressure based on measurements at just one pressure.

Changes in the leading features reflect a change from tetrahedral to octahedral oxygen coordination around the W atoms, with an increase in the crystal-field splitting and the well-known reversal of orbital ordering/degeneracy of the W 5*d* orbitals: approximately E and T_2 in tetrahedral symmetry versus T_{2g} and E_g in octahedral symmetry [32]. The crystal-field splitting of the W 5*d* T_{2g} and E_g states in the $PbWO_4$-III phase is found to be about 4.1 eV, as measured by the separation of the two peaks that compose the white line. This splitting was not resolved in a previous conventional x-ray absorption fine-structure measurement [17,19]. The smaller splitting of the E and T_2 orbitals is not resolved in the $PbWO_4$-I phase, although the white line has two components. They are clearly seen in our calculated spectra if lifetime broadening is artificially omitted. The change in the relative intensity of these features is consistent with the reversal of the orbital degeneracy for tetrahedral versus octahedral symmetry. Another notable feature is the broad peak near 10 222.5 eV at 0 GPa (1 bar), which decreases abruptly in intensity around the phase-transition at 7.2 GPa, and it continues to decrease and shift in energy with increasing pressure.

Pb L_3 HERFD near-edge spectra are shown in the right panel of Fig. 2. Spectral features reveal unoccupied Pb 6*s* and 6*d* states. The spectra show modest changes from 0 GPa (1 bar) up to 6.2 GPa, and there is a significant change by 7.2 GPa with only slight changes found thereafter. However, unlike the W L_3 edge HERFD data, a pre-edge feature near 13030 eV is also observed. The intensity of this pre-edge feature increases up to 6.2 GPa but increases more rapidly above 7.2 GPa. The first major peak around 13 042 eV is stable in both intensity and position throughout the entire high-pressure range. On the other hand, the peak around 13 050 eV is constant from 0 GPa (1 bar) up to 6.2 GPa, but it decreases abruptly by 7.2 GPa with a further decrease in intensity and shifts to higher energy with increasing pressure. Significant differences are also observed with pressure in the region near and above 13 060 eV that are also consistent with the transition between the $PbWO_4$-I and $PbWO_4$-III phases.

Linear-combination fits of both the Pb and W HERFD spectra around the phase-transition pressure were also performed. We found that the phase transition begins at 7.2 GPa (approximately 50% of the sample had transformed into the $PbWO_4$-III phase) and was fully completed at 8.1 GPa.

IV. THEORY AND DISCUSSION

Crystal structures used to simulate the spectra were predicted using DFT calculations performed with the VASP code, [33–35] version 5.4.4. We used the projected augmented wave Perdew-Burke-Ernzerhof (PBE) pseudopotentials [36,37] Pb_*d*, W_sv, and O from the VASP 5.4 pseudopotential library. We also used a plane wave cut-off energy of 500 eV and a Γ-centered *k*-point grid whose dimension in each reciprocal-lattice direction was the integer most consistent with an effective 24-Å supercell periodicity [38,39].

Various choices for the exchange-correlation functional were tested for the ability to reproduce experimental α-PbO [40] and triclinic WO_3 [41] crystal structures. The PBE functional [42] tended to overestimate lattice parameters, as is well known. The choices that reproduced the experimental lattice parameters and atomic positions most accurately were the dispersion-corrected optB86b-van der Waals (vdW) functional [43,44] and the meta generalized gradient approximation Strongly Constrained and Appropriately Normed (SCAN) functional [45]. Remarkably, even better structural accuracy was achieved by sacrificing self-consistency and taking the average of the optB86b-vdW and SCAN structures. For the optimized $PbWO_4$ structures, we independently minimized the enthalpy for a given structure type under pressure using the optB86b-vdW and SCAN functional, and we averaged the structures obtained. The results are shown in Table I with the corresponding published crystal structural parameters.

We also calculated the relative enthalpy of the different common $PbWO_4$ phases as a function of pressure using various choices of density functionals. The key results, along with other results from the literature, are shown in Table II, alongside the energy-volume per formula unit curves (Fig. 3). All functionals agree that the high-pressure phase of $PbWO_4$ is the $PbWO_4$-III phase, and that the $PbWO_4$-I to $PbWO_4$-III transition occurs at lower pressure than the pressure where the $PbWO_4$-I to Fergusonite structure transition would occur. The various functionals disagree as to whether $PbWO_4$-I or

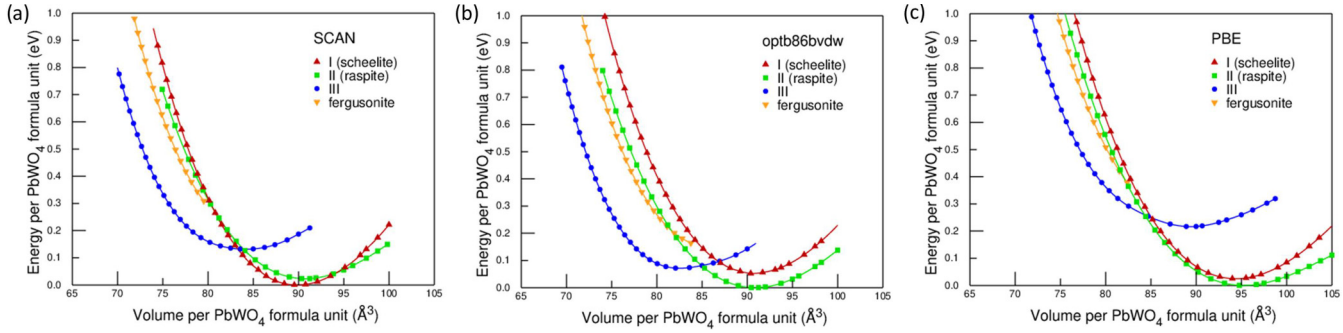

FIG. 3. Calculated enthalpy versus volume curves for $PbWO_4$-I (I), $PbWO_4$-II (II), $PbWO_4$-III (III) and Fergusonite structures using the SCAN (a), opt86bvdW (b), and PBE functionals (c).

$PbWO_4$-II has the lowest enthalpy at low pressure and disagree by several GPa as to the values of transition pressures. The optB86bvdW functional seems to predict particularly low transition pressures. The results show that discrepancies of the order of 10 meV per atom for relative $PbWO_4$ phase stability exist among the state-of-the-art density functionals.

In our calculations, we made the approximation that HERFD spectra would be proportional to XAS. This assumes that the HERFD branching ratio is independent of excitation energy. Furthermore, the calculations relied on solving the Bethe-Salpeter equation (BSE) using the OCEAN program. [46] OCEAN can treat spin-orbit effects. In this case, however, the large L_2-L_3 spin-orbit splittings permitted neglect of spin-orbit effects and multiplication of spectral features by 3/5. Spectral features were broadened using the reported measured resolution and theoretical broadening of the unoccupied states. The theoretical broadening included a model self-energy calculation [47] plus additional broadening of 1.0 eV (FWHM, and judged by examining spectra) applied to the W 5*d* E_g states in $PbWO_4$-III to account for E-e Jahn-Teller interactions. Without this last adjustment, which proved necessary, the E_g peaks were too narrow and sharply peaked.

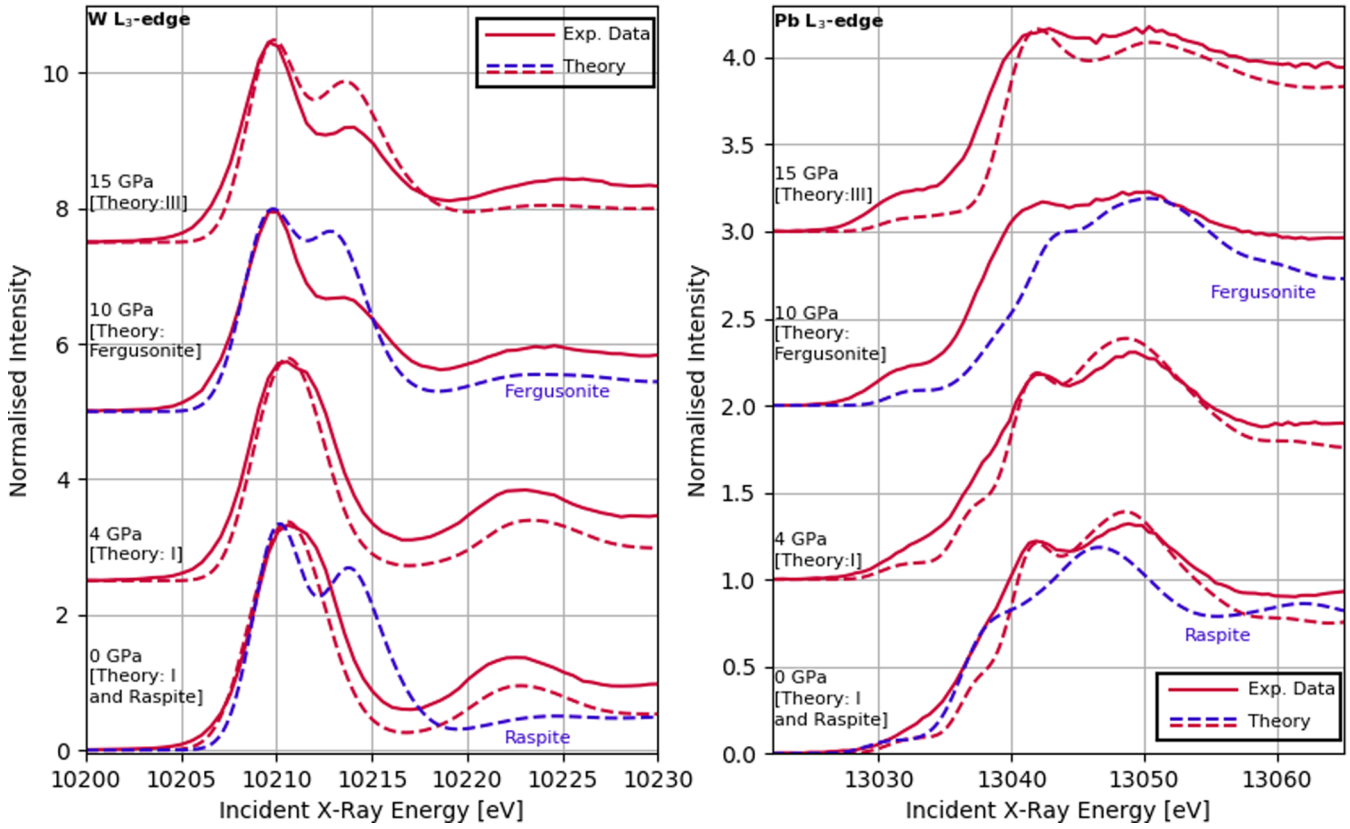

FIG. 4. (Left/Right panels) High pressure W/Pb L_3 absorption-edge experimental data (solid red curves, Exp. Data) and BSE+DFT theory for $PbWO_4$ (dashed red curves). The dashed blue curves represent theory for Raspite and Fergusonite structures which are ruled out as candidate structures based on the experimental data. Theory I and Theory III denote theoretical calculations for the $PbWO_4$ Phase-I and Phase-III structures, respectively. The noted pressures are those used for the theoretical calculations. The corresponding experimental pressures were 1bar, 4.2 GPa, 9.7 GPa, and 14.9 GPa.

TABLE III. DFT structures used as input for selected pressure-dependent simulated absorption spectra (Fig. 4). The $PbWO_4$-II (Raspite) structure at $P = 0$ GPa used is given in Table I.

		DFT $PbWO_4$-I DFT at 4 GPa (optb86bvdw+SCAN average) $a = 5.4127$ Å, $c = 11.7154$ Å		
Atom	Site	x	y	z
Pb	4b	0	0.25	0.625
W	4a	0	0.25	0.125
O	16f	0.2309	0.0985	0.0399
		DFT $PbWO_4$ (Fergusonite-type structure) at 10 GPa (optb86bvdw+SCAN average) $I2/a$, $Z = 4$, $a = 5.9047$ Å, $b = 10.8946$ Å, $c = 4.8667$ Å, $\beta = 97.162°$		
Atom	Site	x	y	z
Pb	4e	0.25	0.6186	0
W	4e	0.25	0.1518	0
O_1	8f	0.9064	0.9576	0.2259
O_2	8f	0.4504	0.2108	0.7622
		$PbWO_4$-III at 15 GPa (optb86bvdw+SCAN average) $P2_1/n$, $Z = 8$, $a = 11.9781$ Å, $b = 6.7444$ Å, $c = 7.1547$ Å, $\beta = 89.246°$		
Atom	Site	x	y	z
Pb_1	4e	0.1599	0.6751	0.1660
Pb_2	4e	0.1322	0.9634	0.6212
W_1	4e	0.0862	0.1687	0.0792
W_2	4e	0.0988	0.4697	0.6433
O_1	4e	0.1055	0.0199	0.2861
O_2	4e	0.1983	0.6119	0.7714
O_3	4e	0.0455	0.6636	0.4743
O_4	4e	0.2254	0.2730	0.0666
O_5	4e	0.0694	0.2621	0.8119
O_6	4e	0.1857	0.3471	0.4784
O_7	4e	0.0198	0.3899	0.1789
O_8	4e	0.0839	0.9116	0.9480

The BSE calculations assumed the structures obtained from the DFT calculations but used the local-density approximation to build up required Bloch functions. While this choice of functional is not consistent with those used for modeling the structures, the choice of functional is not important for such core-excitation spectrum calculations in $PbWO_4$. We used hard, norm-conserving pseudopotentials of the Hamann-Schlüter-Chiang type [48] with Vanderbilt cut-off functions [49]. We used O^{6+}, W^{6+} and Pb^{4+} cores and a 1361 eV plane-wave cut-off for band states. The calculations included 245, 495, and 795 bands for systems having 12 ($PbWO_4$-I and the Fergusonite phase), 24 ($PbWO_4$-II), and 48 ($PbWO_4$-III) atoms per primitive unit cell. These bands accounted for the states present in the spectral regions shown.

The results of the BSE calculations are shown in Fig. 4, along with associated experimental spectra for comparison. Only several pressures are shown well above and well below the measured experimental phase transition for clarity. The structural parameters obtained from our DFT calculations for these data are reported in Table III. It was found that only very small changes to the theoretical spectra occurred within the individual phases as a function of pressure, which is consistent with the behavior of the observed spectra. The W L_3 absorption edge calculated spectra (Fig. 4 left panel) are shown together with the experimental HERFD spectra. The crystal-field splitting because of the W octahedral coordination in the high-pressure $PbWO_4$-III phase is reproduced, together with the broad peak feature above 10220 eV. The Pb L_3 absorption edge calculation spectra (Fig. 4 right panel) are also shown together with the experimental HERFD spectra. An excellent agreement between experiment and theory is clearly seen above 13040 eV. Also shown, together with experimental HERFD data, are the Raspite and Fergusonite phases calculated at 0 and 10 GPa, respectively. Raspite also features octahedral coordination of the tungsten and a concomitant crystal-field splitting indicated in its BSE calculations. From these results, Raspite is ruled out as being the ambient pressure phase of $PbWO_4$. Likewise, the ligand-field splitting of the Fergusonite structure is too small (3.1 eV) to consider it as the high-pressure phase candidate. In the case of Pb, the Raspite and Fergusonite structure BSE spectra also bear little resemblance to measured spectra, so that these phases can be ruled out as having been either observed or created in the experiment.

V. CONCLUSION

Using both DFT and theoretical XAS that incorporate BSE treatment, and combining them with high resolution experimental spectra, the high-pressure phase transition from

$PbWO_4$-I to $PbWO_4$-III at around 7 GPa was convincingly established. The combined results of experiment, DFT calculations of enthalpies of formation, and BSE calculations of HERFD spectra at both the W and Pb L_3 absorption edges were all required to provide the most complete interpretation of the data. The higher energy resolution afforded by the HERFD method as compared to XAS for core excitation spectroscopy and the ability to eliminate broadening mechanisms in theoretical spectra greatly clarified these findings.

Regarding DFT enthalpies of formation, it is hard to determine whether $PbWO_4$-I or $PbWO_4$-II is favored at lower pressure, but BSE spectra compared to the low-pressure HERFD-spectra definitively favor $PbWO_4$-I over $PbWO_4$-II. This is still to be marked as a successful result for DFT, which nonetheless provided atomic coordinates in both structures, and it argues for the joint application of different types of analysis (DFT and BSE). A similar comparison of sample BSE spectra for $PbWO_4$-III and the Fergusonite structure rule out the latter as the high-pressure phase, as does a comparison of DFT-based theoretical enthalpies of formation.

ACKNOWLEDGMENTS

We acknowledge SOLEIL and the GALAXIES beamline for provision of synchrotron radiation facilities (Proposal No. 20161496). Additional support was provided by the Natural Sciences and Engineering Research Council of Canada (2019-06818).

[1] T. C. E. C. Group, P. Adzic, N. Almeida, D. Andelin, R. Y. Zhu *et al.*, Radiation hardness qualification of $PbWO_4$ scintillation crystals for the CMS electromagnetic calorimeter, J. Inst. **5**, P03010 (2010).

[2] A. A. Kaminskii, C. L. McCray, H. R. Lee, S. W. Lee, D. A. Temple, T. H. Chyba, W. D. Marsh, J. C. Barnes, A. N. Annanenkov, V. D. Legun, H. J. Eichler, G. M. A. Gad, and K. Ueda, High efficiency nanosecond raman lasers based on tetragonal $PbWO_4$ crystals, Opt. Commun. **183**, 277 (2000).

[3] P. S. Walke, V. B. Patil, I. S. Mulla, and D. J. Late, High performance single crystalline $PbWO_4$ nanorod field effect transistor, J. Mater. Sci.: Mater. Electron. **26**, 10044 (2015).

[4] S. Li, R. Ahuja, Y. Wang, and B. Johansson, Crystallographic structures of $PbWO_4$, High Pressure Res. **23**, 343 (2003).

[5] J. Yang, C. Lu, H. Su, J. Ma, H. Cheng, and L. Qi, Morphological and structural modulation of $PbWO_4$ crystals directed by dextrans, Nanotechnology **19**, 035608 (2008).

[6] J. M. Moreau, P.h. Galez, J. P. Peigneux, and M. V. Korzhik, Structural characterization of $PbWO_4$ and related new phase $Pb_7W_8O_{(32-x)}$, J. Alloys. Compd. **238**, 46 (1996).

[7] D. Tan, W. Xiao, W. Zhou, M. Chen, W. Zhou, and J. Xu, Effects of pressure on $PbWO_4$-III, Phys. Chem. Miner. **40**, 341 (2013).

[8] P. W. Richter, G. J. Kruger, and C. W. F. T. Pistorius, $PbWO_4$-III (a high-pressure form), Acta Crystallogr. B **32**, 928 (1976).

[9] R. Chipaux, G. André, and A. Cousson, Crystal structure of lead tungstate at 1.4 and 300 K, J. Alloys. Compd. **325**, 91 (2001).

[10] A. Grzechnik, W. A. Crichton, W. G. Marshall, and K. Friese, High-pressure x-ray and neutron powder diffraction study of $PbWO_4$ and $BaWO_4$ scheelites, J. Phys.: Condens. Matter **18**, 3017 (2006).

[11] R. Lacomba-Perales, D. Errandonea, A. Segura, J. Ruiz-Fuertes, P. Rodríguez-Hernández, S. Radescu, J. López-Solano, A. Mujica, and A. Muñoz, A combined high-pressure experimental and theoretical study of the electronic band-structure of scheelite-type AWO_4 (A = Ca, Sr, Ba, Pb) compounds, J. Appl. Phys. **110**, 043703 (2011).

[12] R. Lacomba-Perales, J. Ruiz-Fuertes, D. Errandonea, D. Martínez-García, and A. Segura, Optical absorption of divalent metal tungstates: correlation between the band-gap energy and the cation ionic radius, Europhys. Lett. **83**, 37002 (2008).

[13] R. M. Hazen, L. W. Finger, and J. W. E. Mariathasan, High-pressure crystal chemistry of scheelite-type tungstates and molybdates, J. Phys. Chem. Solids **46**, 253 (1985).

[14] J. López-Solano, P. Rodríguez-Hernández, S. Radescu, A. Mujica, A. Muñoz, D. Errandonea, F. J. Manjón, J. Pellicer-Porres, N. Garro, A. Segura, C. H. Ferrer-Roca, R. S. Kumar, O. Tschauner, and G. Aquilanti, Crystal stability and pressure-induced phase transitions in scheelite AWO_4 (A = Ca, Sr, Ba, Pb, Eu) binary oxides. I: A review of recent ab initio calculations, ADXRD, XANES, and raman studies, Phys. Status Solidi B **244**, 325 (2007).

[15] D. Christofilos, E. Efthimiopoulos, J. Arvanitidis, K. Papagelis, S. Ves, and G. A. Kourouklis, Raman study of polycrystalline $PbWO_4$ under high pressure, High Pressure Res. **26**, 421 (2006).

[16] F. J. Manjon, D. Errandonea, N. Garro, J. Pellicer-Porres, J. López-Solano, P. Rodríguez-Hernández, S. Radescu, A. Mujica, and A. Muñoz, Lattice dynamics study of scheelite tungstates under high pressure II. $PbWO_4$, Phys. Rev. B **74**, 144112 (2006).

[17] D. Errandonea and F. J. Manjón, Pressure effects on the structural and electronic properties of ABX_4 scintillating crystals, Prog. Mater. Sci. **53**, 711 (2008).

[18] D. Errandonea, K. K. Mishra, and A. Polian, In-situ high-pressure raman scattering studies in $PbWO_4$ up to 48 GPa, J. Alloys. Compd. **667**, 36 (2016).

[19] D. Errandonea, J. Pellicer-Porres, F. J. Manjón, A. Segura, C.h. Ferrer-Roca, R. S. Kumar, O. Tschauner, J. López-Solano, P. Rodríguez-Hernández, S. Radescu, A. Mujica, A. Muñoz, and G. Aquilanti, Determination of the high-pressure crystal structure of $BaWO_4$ and $PbWO_4$, Phys. Rev. B **73**, 224103 (2006).

[20] P. Glatzel, T.-C. Weng, K. Kvashnina, J. Swarbrick, M. Sikora, E. Gallo, N. Smolentsev, and R. A. Mori, Reflections on hard x-ray photon-in/photon-out spectroscopy for electronic structure studies, J. Electron. Spectrosc. Relat. Phenom. **188**, 17 (2013).

[21] S. Lafuerza, M. Retegan, B. Detlefs, R. Chatterjee, V. Yachandra, J. Yano, and P. Glatzel, New reflections on hard x-ray photon-in/photon-out spectroscopy, Nanoscale **12**, 16270 (2020).

[22] K. Hämäläinen, D. P. Siddons, J. B. Hastings, and L. E. Berman, Elimination of the Inner-Shell Lifetime Broadening in x-Ray-Absorption Spectroscopy, Phys. Rev. Lett. **67**, 2850 (1991).

[23] J. C. Swarbrick, U. Skyllberg, T. Karlsson, and P. Glatzel, High energy resolution x-ray absorption spectroscopy of environmentally relevant lead(ii) compounds, Inorg. Chem. **48**, 10748 (2009).

[24] J. M. Ablett, D. Prieur, D. Céolin, B. Lassalle-Kaiser, B. Lebert, M. Sauvage, T.h. Moreno, S. Bac, V. Balédent, A. Ovono, M. Morand, F. Gélebart, A. Shukla, and J.-P. Rueff, The GALAXIES inelastic hard x-ray scattering end-station at synchrotron SOLEIL, J. Synchrotron Radiat. **26**, 263 (2019).

[25] J.-P. Rueff, J. M. Ablett, D. Céolin, D. Prieur, T. Moreno, V. Balédent, B. Lassalle-Kaiser, J. E. Rault, M. Simon, and A. Shukla, The GALAXIES beamline at the SOLEIL synchrotron: inelastic x-ray scattering and photoelectron spectroscopy in the hard x-ray range, J. Synchrotron Radiat. **22**, 175 (2015).

[26] A. Jayaraman, B. Batlogg, and L. G. VanUitert, Effect of high pressure on the raman and electronic absorption spectra of $PbMoO_4$ and $PbWO_4$, Phys. Rev. B **31**, 5423 (1985).

[27] S. Klotz, J.-C. Chervin, P. Munsch, and G. L.e Marchand, Hydrostatic limits of 11 pressure transmitting media, J. Phys. D **42**, 075413 (2009).

[28] D. D. Ragan, D. R. Clarke, and D. Schiferl, Silicone fluid as a high-pressure medium in diamond anvil cells, Rev. Sci. Instrum. **67**, 494 (1996).

[29] K. Takemura, Evaluation of the hydrostaticity of a helium-pressure medium with powder x-ray diffraction techniques, J. Appl. Phys. **89**, 662 (2001).

[30] H. K. Mao, J. Xu, and P. M. Bell, Calibration of the ruby pressure gauge to 800 kbar under quasi-hydrostatic conditions, J. Geophys. Res. **91**, 4673 (1986).

[31] J. M. Ablett, J. C. Woicik, and C. C. Kao, New correction procedure for x-ray spectroscopic fluorescence data: simulations and experiment., international centre for diffraction data, Adv. X-Ray Anal. **48**, 266 (2005).

[32] F. A. Cotton, *Chemical Applications of Group Theory*, 3rd ed. (Wiley, New York, 1990).

[33] G. Kresse and J. Furthmüller, Efficiency of ab-initio total energy calculations for metals and semiconductors using a plane-wave basis set, Comput. Mater. Sci. **6**, 15 (1996).

[34] G. Kresse and J. Furthmüller, Efficient iterative schemes for ab initio total-energy calculations using a plane-wave basis set, Phys. Rev. B **54**, 11169 (1996).

[35] Certain commercial software is identified in this paper to adequately describe the methodology used. Such identification does not imply recommendation or endorsement by the National Institute of Standards and Technology, nor does it imply that the software identified is necessarily the best available for the purpose. NIST-developed software is expressly provided "as is." NIST makes no warranty of any kind, express, implied, in fact or arising by operation of law, including, without limitation, the implied warranty of merchantability, fitness for a particular purpose, noninfringement and data accuracy. NIST neither represents nor warrants that the operation of the software will be uninterrupted or error-free, or that any defects will be corrected. NIST does not warrant or make any representations regarding the use of the software or the results thereof, including but not limited to the correctness, accuracy, reliability, or usefulness of the software.

[36] P. E. Blöchl, Projector augmented-wave method, Phys. Rev. B **50**, 17953 (1994).

[37] G. Kresse and D. Joubert, From ultrasoft pseudopotentials to the projector augmented-wave method, Phys. Rev. B **59**, 1758 (1999).

[38] Technically, within VASP, this corresponds to automatic k-point generation with $R_k = 24$ (see https://www.vasp.at/wiki/index.php/KPOINTS).

[39] For example, the DFT calculations used a Γ (origin) centered k-point grid of dimension $4 \times 4 \times 2$, $4 \times 2 \times 5$, $2 \times 5 \times 4$, and $2 \times 4 \times 3$, respectively, for the $PbWO_4$-I at 4 GPa, Fergusonite at 10 GPa, $PbWO_4$-II at 0 GPa and $PbWO_4$-III at 15 GPa structures given in Tables I and III.

[40] J. Leciejewicz, On the crystal structure of tetragonal (red) PbO, Acta Crystallogr. **14**, 1304 (1961).

[41] P. M. Woodward, A. W. Sleight, and T. Vogt, Structure refinement of triclinic tungsten trioxide, J. Phys. Chem. Solids **56**, 1305 (1995).

[42] J. P. Perdew, K. Burke, and M. Ernzerhof, Generalized Gradient Approximation Made Simple, Phys. Rev. Lett. **77**, 3865 (1996).

[43] J. Klimeš, D. R. Bowler, and A. Michaelides, Chemical accuracy for the van der waals density functional, J. Phys.: Condens. Matter **22**, 022201 (2010).

[44] J. Klimeš, D. R. Bowler, and A. Michaelides, Van der waals density functionals applied to solids, Phys. Rev. B **83**, 195131 (2011).

[45] J. Sun, A. Ruzsinszky, and J. P. Perdew, Strongly Constrained and Appropriately Normed Semilocal Density Functional, Phys. Rev. Lett. **115**, 036402 (2015).

[46] K. Gilmore, J. Vinson, E. L. Shirley, D. Prendergast, C. D. Pemmaraju, J. J. Kas, F. D. Vila, and J. J. Rehr, Efficient implementation of core-excitation bethe-salpeter equation calculations, Comput. Phys. Commun. **197**, 109 (2015).

[47] E. L. Shirley, A new model dielectric function for loss functions and electron damping, Radiat. Phys. Chem. **167**, 108165 (2020).

[48] D. R. Hamann, M. Schlüter, and C. Chiang, Norm-Conserving Pseudopotentials, Phys. Rev. Lett. **43**, 1494 (1979).

[49] D. Vanderbilt, Optimally smooth norm-conserving pseudopotentials, Phys. Rev. B **32**, 8412 (1985).

[50] T. Fujita, I. Kawada, and K. Kato, Raspite from broken hill, Acta Crystallogr. B **33**, 162 (1977).